

# Fault healing promotes high-frequency earthquakes in laboratory experiments and on natural faults

Gregory C. McLaskey<sup>†1</sup>, Amanda M. Thomas<sup>2</sup>, Steven D. Glaser<sup>1</sup>, Robert M. Nadeau<sup>2</sup>

**Citation:** McLaskey, G. C., A. M. Thomas, S. D. Glaser, R. M. Nadeau (2012) Fault healing promotes high frequency earthquakes in the laboratory and on natural faults. *Nature*. 491, doi:10.1038/nature11512.

**Faults strengthen or heal with time in stationary contact<sup>1,2</sup>, and this healing may be an essential ingredient for the generation of earthquakes<sup>1-3</sup>. In the laboratory, healing is thought to be the result of thermally activated mechanisms that weld together micrometer sized asperity contacts on the fault surface, but the relationship between laboratory measures of fault healing and seismically observable properties of earthquakes is currently not well defined. Here, we report on laboratory experiments and seismological observations that show how earthquakes vary as a function of healing time. In the laboratory, we find that increased healing causes a disproportionately large amount of high frequency seismic radiation to be produced during fault rupture. We observe a similar connection between earthquake spectra and recurrence time for repeating earthquake sequences on natural faults. Healing rates are dependent upon pressure, temperature<sup>4</sup>, and mineralogy<sup>1</sup>, so the connection between seismicity and healing may help explain recent observations of large megathrust earthquakes which indicate that energetic high frequency seismic radiation originates from locations that are distinct from the geodetically inferred locations of large amplitude fault slip<sup>5-7</sup>.**

In laboratory experiments, static fault frictional strength  $\mu_s$  is generally observed to increase linearly with log of time in stationary contact  $t_{hold}$  according to

$$\mu_s(t_{hold}) = \alpha_s + \beta_s \log_{10}(t_{hold}), \quad (1)$$

where  $\beta_s$  is the healing rate and  $\alpha_s$  is the fault strength at time  $t_{hold} = 1$  s (refs 1-4,8). These measurements are used to derive rate- and state-dependent friction laws<sup>2,3</sup> that have provided insight into fault behavior ranging from slow slip to dynamic rupture<sup>2,8-10</sup>. Healing rates have also been inferred from repeating earthquake sequences<sup>10-12</sup> (RESSs). These are sets of events with nearly identical waveforms, locations, and magnitudes that are thought to represent the repeated rupture of a patch of fault that is slowly loaded by aseismic slip of the surrounding material. Here, we consider the stick-slip of a laboratory fault as a proxy for a fault patch and compare our results to observations of RES on the San Andreas fault. In addition to measuring static friction, slip, and stress drop, we record the stress waves emitted during the rupture of the laboratory fault, termed laboratory earthquakes (LabEQs). This facilitates a link between friction properties observed in the laboratory and earthquakes produced on natural faults.

Fault healing is typically attributed to an increase in either the area or strength of asperity contacts due to “creep”<sup>2,3</sup>. Mechanisms may include stress-induced diffusion, dislocation motion, chemically aided slow crack growth, dissolution-precipitation processes, or other thermally activated processes<sup>2,3,13-15</sup>. While specific mechanisms may differ, the overall effects of healing are remarkably similar. Equation 1 is applicable to rocks<sup>1</sup>, metals<sup>16</sup>, plastics<sup>4</sup>, and paper,<sup>17</sup> which suggests that the mechanics of healing are not

---

<sup>1</sup>Department of Civil and Environmental Engineering, University of California, Berkeley, CA, 94720

<sup>2</sup>Department of Earth and Planetary Science, Berkeley Seismological Laboratory, University of California, Berkeley, CA, 94720.

<sup>†</sup> Now at the United States Geological Survey, 345 Middlefield Rd. MS 977, Menlo Park, CA, USA  
gmclaskey@usgs.gov

greatly dependent on specific chemical or physical properties, but rely on universally observed surface properties such as multi-scale roughness. A better understanding of the relationship between fault healing and earthquake generation may be the key to understanding the physics of earthquakes<sup>18</sup>.

Test blocks are composed of the glassy polymer poly(methyl methacrylate) (PMMA). PMMA and similar glassy polymers are commonly used as model materials for fault rupture and friction studies<sup>2,4,19,20</sup>. Friction on PMMA/PMMA interfaces obeys Equation 1 and is well modeled by the rate- and state-dependent friction laws<sup>2,4</sup>. Because of its low hardness and melting temperature ( $\sim 160^\circ\text{C}$ ), the behavior of PMMA/PMMA interfaces at room temperature and modest stress levels (100 kPa) may be somewhat representative of the behavior of rocks at depth<sup>20</sup>. The similarities and differences between plastic and rock may serve as important points of comparison when studying the range of friction properties expected in the brittle-ductile spectrum of crustal deformation behavior.

Stick-slip experiments were conducted at room temperature and humidity on a direct shear apparatus consisting of a PMMA slider block (181 mm long by 60 mm wide by 17 mm high) and a larger PMMA base plate (450 mm by 300 mm by 36 mm) shown in Figure 1a (inset). With normal force  $F_N$  held constant, shear force  $F_S$  is increased until the sample undergoes a series of stick-slip instabilities, denoted events. Recurrence time,  $t_r$ , defined as the time since the previous event, is computed for each time-adjacent pair of events in the sequence. (Despite subtle differences<sup>21</sup>, we assume  $t_r = t_{\text{hold}}$  from slide-hold-slide laboratory experiments and Equation 1.) Each event produces a LabEQ, which is recorded with piezoelectric sensors attached to the PMMA base plate. The slider block slips 50 - 200  $\mu\text{m}$  during each event. Some slow premonitory slip ( $\sim 2 \mu\text{m}$ ) is often detected 1-2 ms before rapid slip commences. We detect no slip between events (to  $\sim 1 \mu\text{m}$  noise level). The duration of slip for each event is approximately constant (8 ms), and is likely controlled by the combined stiffness of the apparatus and samples rather than fault rupture properties.

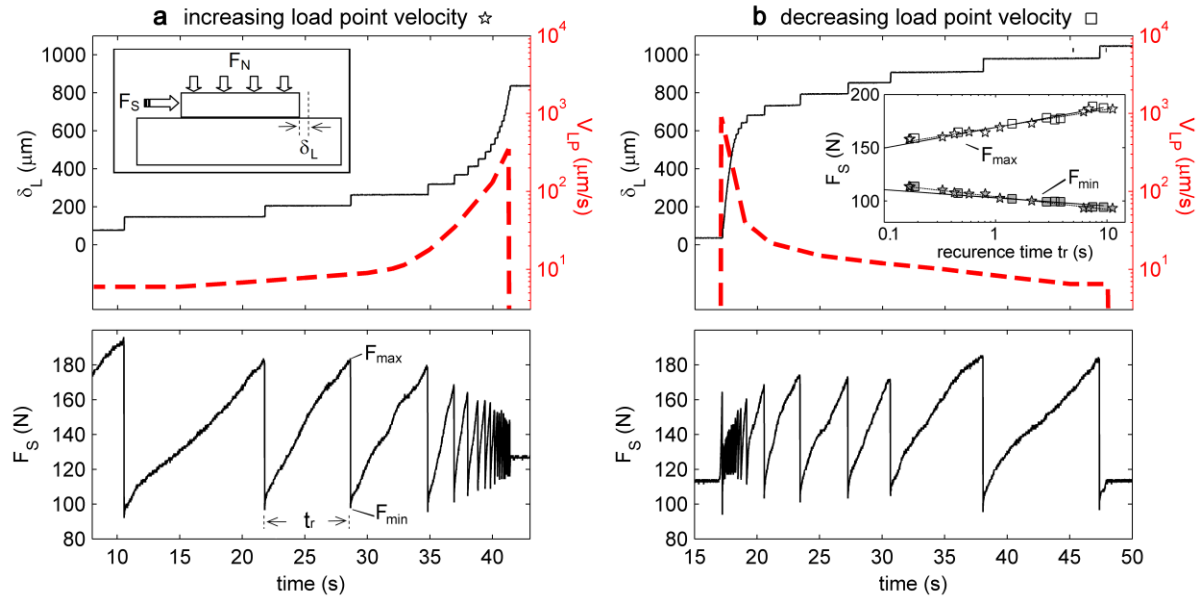


**Figure 1. Experimental data from a pair of healing tests.** Shear force  $F_S$ , load point velocity  $v_{LP}$  (dashed line), and slip  $\delta_L$ , measured from stick-slip experiments at  $\sigma_n = 36$  kPa. All experiments were conducted in pairs, one with increasing  $v_{LP}$  (a), and one with decreasing  $v_{LP}$  (b) Left inset: schematic of the apparatus. Right inset: the maximum shear force  $F_{\max}$  and minimum shear force  $F_{\min}$  were measured for each event in the stick-slip sequence and are plotted against the logarithm of the recurrence time ( $t_r$ ). Stars and squares are from runs with increasing and decreasing  $v_{LP}$ , respectively.

Load point displacement  $x_{LP}$  is controlled by turning a fine threaded screw that presses against the trailing edge of the slider block. When load point velocity,  $v_{LP} = d(x_{LP})/dt$ , is systematically increased or decreased, large variations in  $t_r$  can be achieved on a single experimental run, while other experimental variables ( $F_N$ , surface conditions, etc.) are kept constant. Typical results are shown in Figure 1. To isolate cumulative wear and loading rate effects, experimental runs were conducted in pairs: one with increasing  $v_{LP}$  (Figure 1a) and one with decreasing  $v_{LP}$  (Figure 1b). For every event in each stick-slip sequence, we measure  $F_{max}$  and  $F_{min}$  (see Figure 1) and calculate stress drop  $\Delta\tau = (F_{max} - F_{min})/A$ , where  $A$  is the nominal fault area (.0109 m<sup>2</sup>). These parameters are plotted against  $\log_{10}(t_r)$  (Figure 1(b) inset; Supplementary Figures S2-S4). Slopes,  $\beta$ , and intercepts,  $\alpha$ , of the best fit lines are reported in Supplementary Table S1. All tests show results consistent with Equation 1 and previous work<sup>1,3,4,8</sup>. The increase in  $\Delta\tau$  with increasing  $t_r$  is due to both an increase in  $F_{max}$  and a decrease in  $F_{min}$  with  $\log_{10}(t_r)$ <sup>8,21</sup>. In all cases, healing rates  $\beta$  are slightly larger for runs with decreasing  $v_{LP}$  compared to runs with increasing  $v_{LP}$ , indicating dependence on loading rate or stress time history.

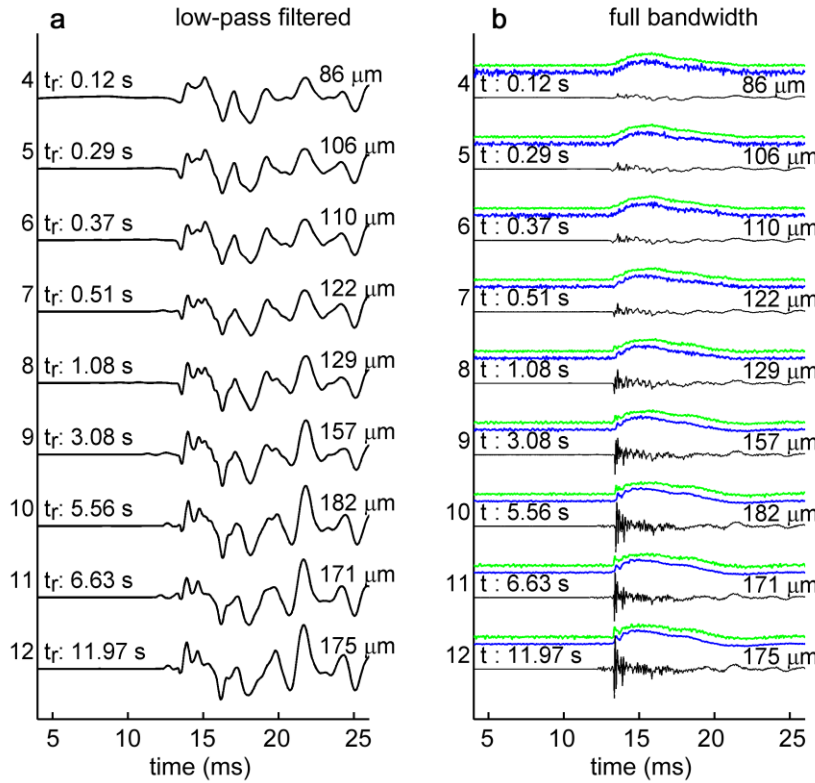


**Figure 2: Sequence of successive LabEQs.** Events from an experimental run with decreasing load point velocity (increasing time between successive events) at  $\sigma_n = 130$  kPa and using a rough sample (Run 45-R-Dec; see Supplementary Table S1). Each trace is scaled by the total measured slip  $\delta_f$ , printed on each trace. **a**, Signals are low-pass filtered (1 kHz cutoff) to illustrate similarity of low frequency waveforms. **b**, Full bandwidth recorded LabEQ (raw sensor output) plotted alongside scaled slip rates  $(d\delta_f/dt)/\delta_f$  which are derived from slip measured at the leading (blue) and trailing edges (green) of the slider block, and low-pass filtered at 5 kHz to reduce high frequency noise. The green curves have the same scale as the blue curves, and are offset for clarity.

An example sequence of LabEQ seismograms is shown in Figure 2. The interface properties, apparatus/specimen stiffness, sensor response, and wave propagation characteristics do not change between successive events, so differences between LabEQs are attributed to variations in the  $t_r$ . When each seismogram is scaled to total measured slip,  $\delta_f$ , the low frequency components (Figure 2a) are nearly identical, but the high frequency components (Figure 2b) depend strongly on  $t_r$ . Absolute source spectra were estimated for each LabEQ by removing the instrument and apparatus response functions from recorded signals by means of a ball drop calibration source (see Methods). Examples of absolute source displacement spectra are shown in Figure 3a for three LabEQs from Figure 2. Each source spectra is roughly linear with  $\log(\omega)$ , so spectra are fitted with a best fit line. Variations in spectral slopes of LabEQ source spectra are shown in Figure 3b for all 46 events from four tests conducted at normal stress  $\sigma_n = 130$  kPa. These laboratory results show a disproportionate increase in high-frequency ground motions with longer  $t_r$ . Similar spectral changes were observed for all experiments, but are most pronounced for

those conducted at higher  $\sigma_n$ . Peak high frequency ground motions coincide with the initiation of slip, not maximum slip rate.

To complement the laboratory results, we analyzed RES on the San Andreas fault<sup>22,23</sup> that were perturbed by the 2004 M6 Parkfield earthquake. As shown in Figure 4, an increase in high frequencies with increasing  $t_r$  was observed for most RES. Similar trends were found for the CA1 RES on the Calaveras fault<sup>11</sup>. If spectral changes were due to a propagation effect, such as damage from the Parkfield earthquake, we would expect to see the effects more pronounced on recordings from source-station ray paths that traverse long distances through zones of expected damage<sup>24</sup> (i.e., near or within the fault zone and at shallower depth)(Supplementary Figure S6, Table S2). Instead, many stations see similar spectral variations between the same events and spectral changes vary among RES (Supplementary Figure S1), so we suspect spectral variations are dominantly controlled by changes in earthquake source characteristics and not path effects.

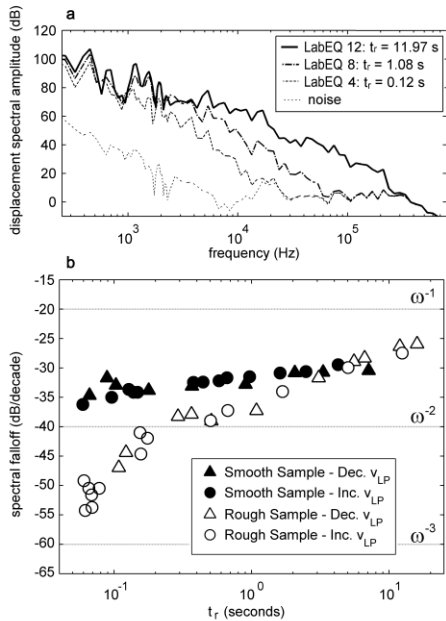


**Figure 3. LabEQ spectral changes with recurrence time.** **a**, Source displacement spectra and the noise spectrum from three of the LabEQs shown in Figure 2 which span two orders of magnitude in  $t_r$ . **b**, the slope of source spectra as a function of recurrence time for all LabEQs from four experimental runs conducted at  $\sigma_n = 130$  kPa. Only the frequency band with a signal-to-noise ratio greater than 6 dB was used for the calculation of these spectral slopes. For the rough sample, spectral slopes increase from  $\omega^{-2.5}$  to  $\omega^{-1.5}$  with increasing  $t_r$ . LabEQs generated from the smooth sample show subtle but systematic spectral changes.

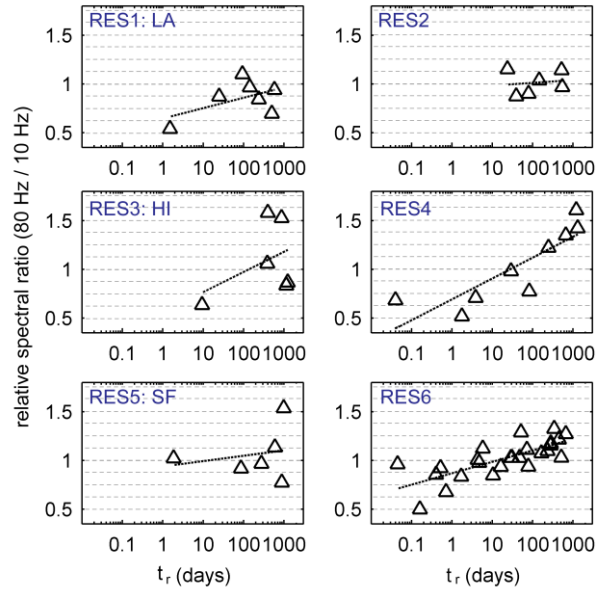


**Figure 4. Spectral changes of RES near Parkfield, CA.** The SF, LA and HI RES were targeted for penetration by the SAFOD deep drilling experiment (sequences NW, SE and S1 in Nadeau et al.<sup>23</sup>). Relative spectral ratios are calculated from the ratio of relative spectral amplitudes at 75-85 Hz to those at 5-15 Hz (Supplementary Figure S5, Table S3). Data points denote the average of relative spectral ratios obtained from ground motions recorded from at least three stations for each event in each RES. Dotted lines show a linear best fit to the data, and a positive slope indicates increasing high frequency ground motions (relative to low frequency) with increasing  $\log_{10}(t_r)$ .

Fault healing appears to cause spectral changes over a broad range of frequencies (Figure 3a), so we propose that our observations are applicable not just to the small length scales and high frequencies of LabEQs, but to natural faults and great earthquakes as well. To discuss the underlying mechanisms of these spectral changes, we present a conceptual fault model in which both natural faults and those in the laboratory are composed of a large number of asperity contacts<sup>2,25,26</sup> with a distribution of strengths,

which collectively sum to produce the static fault strength  $\mu_s$ . If the thermally activated healing mechanisms described above cause asperity contacts to strengthen at a rate proportional to the forces they support, then healing would promote a more heterogeneous spatial distribution of fault strength on the asperity scale. When this healed fault ruptures, its heterogeneous fault strength could cause perturbations in slip velocity which would generate high frequency seismic waves<sup>27</sup>. On the other hand, if healing promotes larger stress drop<sup>8,21</sup> or a more abrupt slip weakening behavior, this would promote faster rupture propagation, which could also account for the enhanced high frequencies. This interpretation is consistent with previous workers who argued that spectral changes observed for the CA1 sequence signify shorter source duration, which could be explained by faster rupture propagation<sup>11</sup>.

The spectral changes shown in Figure 3b are somewhat analogous to those in Figure 4, but when comparing the spectra of LabEQs to those from RES, differences in rise time (the time duration a single point on the fault slips seismically) and rupture duration relative to the recorded frequency band should be taken into account. The LabEQ spectra shown in Figure 3 are likely controlled by details of rupture propagation. Though the sample geometry and resolution of the slip sensors do not permit a detailed analysis of dynamic rupture, Figure 2b does show that slip accelerated more rapidly for events that healed longer. In the case of the RES, even the highest frequencies available for analysis (75-85 Hz) may still be too low to contain much information about rupture propagation. Additionally, complicated interaction between rapid, unstable failure of the fault patch and stable slip imposed by slow slip of the surrounding region<sup>9,10</sup> may contribute to added differences between RES at Parkfield and current laboratory analogues.

Dense seismic arrays have facilitated back projection studies of recent megathrust earthquakes that highlight the temporal and spatial complexity of high-frequency seismic radiation and show that sources of high-frequency seismic waves are not spatially correlated with locations of maximum inferred fault slip<sup>5-7</sup>. A mechanism related to fault healing may be responsible for these puzzling observations, particularly for the March 2011 Tohoku earthquake, where high frequencies originated from deeper sections of the fault and contributed to strong ground accelerations felt in eastern Japan. Laboratory experiments on glassy polymers show that healing rate  $\beta$ , increases by an order of magnitude when temperature is elevated close to the glass transition<sup>4</sup>, so it seems possible that variations in healing rate—due to high pressures and temperatures or fault chemistry—could affect fault properties more profoundly than variations in recurrence time. If deeper sections of the fault are more healed than shallower fault sections, this might cause those parts to radiate more high frequency energy when ruptured in a large earthquake.

The healing-related spectral changes observed in this study demonstrate how earthquake spectra are not simply determined by static fault strength or total fault slip, but by the manner in which slip occurs. Fault sections that heal rapidly or faults that heal for a long time, such as those associated with intraplate earthquakes in low strain-rate environments, will produce higher frequency earthquakes. In contrast, fault sections composed of materials that do not heal, such as smectite, a clay mineral found in the creeping section of the San Andreas fault<sup>28</sup> and in subduction zones<sup>29</sup>, will slip slowly and smoothly.

## Methods (Online only)

**Laboratory:** Fault slip  $\delta$  is measured at both leading ( $\delta_L$ ) and trailing edges ( $\delta_T$ ) of the slider block with eddy current sensors mounted on the samples.  $F_S$  is measured with a load cell located between the loading screw and the slider block. The loading screw is turned by hand. Consequently,  $v_{LP}$  is not precisely controlled but is measured from  $\delta_T$ ,  $F_S$ , and the apparatus/specimen stiffness which was constant for each run. Hydraulic cylinders apply  $F_N$ . Sliding surfaces were milled flat and then roughened by hand lapping with either #60 grit or #600 grit abrasive, producing surface roughness referred to as rough and smooth, respectively.  $F_S$ ,  $\delta_L$ , and  $\delta_T$  are recorded at 2 kHz throughout the experiment. A second system records LabEQs,  $F_S$ ,  $\delta_L$ , and  $\delta_T$  at 2 MHz, for 262 ms surrounding each event or set of events.

**Spectral analysis:** Power spectral estimates (PSEs) were obtained by Fourier transforming a 65.5 ms (lab) or 3.5–4 s (field) signal centered on the first arrival and tapered with a Blackman Harris window. Noise spectra were obtained similarly from signals recorded prior to the first arrival (field) or prior to the first event in each sequence (lab). Only data with signal to noise of at least 6 dB was used. LabEQs were recorded with a Panametrics V103 sensor located 80 mm from the laboratory fault, and absolute source spectra were obtained by dividing PSEs by the PSE of a ball drop calibration source (the stress waves due to a tiny ball impacting the base plate) which has a known source spectrum<sup>30</sup>. Variations in spectra from ball drop sources at different locations on the specimen indicate that absolute source spectra of LABEQs are accurate to  $\pm 8$  dB, while precision is better than  $\pm 2$  dB. RES near Parkfield, CA were recorded as 250 Hz velocity seismograms by the borehole High Resolution Seismic Network (HRSN). Only vertical component records were utilized for this study. RES detections and locations follow Nadeau and McEvilly<sup>22</sup>. For each station and each RES, station averages are calculated by linearly averaging spectra from events cleanly recorded by all stations. We compute relative spectral amplitudes by dividing spectra of individual recordings by the station average. Relative spectral ratios are obtained from the ratio of relative spectral amplitudes at high frequencies (75–85 Hz) to those at lower frequencies (5–15 Hz). A different choice of frequency band (e.g. 65–75 Hz) does not significantly affect the results.

## References

1. Dieterich, J. H. (1972), Time-dependent friction in rocks, *J. Geophys. Res.* **77**, 3690–3697.
2. Dieterich, J. H., & Kilgore, B. D. Direct observations of frictional contacts—new insights for state-dependent properties, *Pure Appl. Geophys.* **143**, 283–302 (1994).
3. Scholz, C. *The Mechanics of Earthquakes and Faulting*, Cambridge University Press, Cambridge (2002).
4. Berthoud, P., Baumberger, T. G'Sell, C. & Hiver, J.-M. Physical analysis of the state- and rate-dependent friction law: Static friction, *Physical Review B* **59**, 14313–14327 (1999).
5. Kiser, E., & Ishii, M. The 2010 Mw 8.8 Chile earthquake: Triggering on multiple segments and frequency-dependent rupture behavior, *Geophys. Res. Lett.* **38**, L07301, doi:10.1029/2011GL047140, (2011).
6. Lay, T., et al. Depth-varying rupture properties of subduction zone megathrust faults, *J. Geophys. Res.*, **117**, B04311 (2012). doi:10.1029/2011JB009133
7. Meng, L., Inbal, A. & Ampuero, J.-P. A window into the complexity of the dynamic rupture of the 2011 Mw 9 Tohoku-Oki earthquake, *Geophys. Res. Lett.* **38**, L00G07 (2011).
8. Karner, S. L., & Marone, C. Effects of loading rate and normal stress on stress drop and stick-slip recurrence interval, in *Geocomplexity and the Physics of Earthquakes*, Geophys. Monogr. Ser., vol. 120, edited by J. B. Rundle, D. Turcotte, and W. Klein, pp. 187 – 198, AGU, Washington, D. C. (2000).
9. Chen, T., & Lapusta, N. Scaling of small repeating earthquakes explained by interaction of seismic and aseismic slip in a rate and state fault model, *J. Geophysical Res.* **114**, B01311 (2009) .
10. Chen, K. H., Bürgmann, R., Nadeau, R. M., Chen, T. & Lapusta, N., Postseismic variations in seismic moment and recurrence interval of repeating earthquakes, *Earth Planet. Sci. Lett.*, **299**, 118–125, (2010).
11. Vidale, J. E., Ellsworth, W. L., Cole, A. & Marone, C. Variations in rupture process with recurrence interval in a repeated small earthquake, *Nature* **368**, 624–626. (1994).
12. Peng, Z., Vidale, J. E. Marone, C. & Rubin, A. Systematic variations in recurrence interval and moment of repeating aftershocks, *Geophys. Res. Lett.* **32**, L15301 (2005).
13. Dieterich J.H., & Conrad, G. Effect of humidity on time and velocity-dependent friction in rocks. *J. Geophys. Res.* **89**, 4196–202 (1984).
14. Cox, S. F., & Paterson M. S. Experimental dissolution precipitation creep in quartz aggregates at high temperatures, *Geophys. Res. Lett.* **18**, 1401–1404 (1991).
15. Li, Q., Tullis, T. E. , Goldsby, D., & Carpick, R. W. Frictional ageing from interfacial bonding and the origins of rate and state friction, *Nature*. **480**, 233–236 (2011).
16. Rabinowitz, E. *Friction and Wear of Materials*, John Wiley, New York (1965).
17. Heslot F., Baumberger T., Perrin B., Caroli B. & Caroli, C. Creep, stick–slip, and dry friction dynamics: Experiments and a heuristic model, *Phys. Rev. E* **49** 4973 (1994).

18. Rice, J. R., & Cocco, M. Seismic fault rheology and earthquake dynamics, in *Tectonic Faults: Agents of Change on a Dynamic Earth*, edited by M. R. Handy, G. Hirth, and N. Hovius, pp. 99–137, MIT Press, Cambridge, Mass (2007).
19. Wu, F.T., Thomson, K.C., & Kuenzler, H. Stick-slip propagation velocity and seismic source mechanism, *Bull. Seismol. Soc. Am.* **62**, 1621-1628 (1972).
20. McLaskey, G. C. & Glaser, S. D. Micromechanics of asperity rupture during laboratory stick slip experiments *Geophys. Res. Lett.* **38**, L12302 (2011).
21. Beeler, N. M., Hickman, S. H., & Wong, T.-f. Earthquake stress drop and laboratory-inferred interseismic strength recovery, *J. Geophys. Res.* **106**, 30,701-30,713 (2001).
22. Nadeau, R. M. & McEvilly, T. V. Fault slip rates at depth from recurrence intervals of repeating microearthquakes, *Science* **285**, 718-721 (1999).
23. Nadeau, R. M., Michalini, A., Uhrhammer, R. A., Dolenc, D. & McEvilly, T. V. Detailed kinematics, structure and recurrence of micro-seismicity in the SAFOD target region
24. Rubinstein, J.L. & Beroza, G.C. Depth constraints on nonlinear strong ground motion, *Geophys. Res. Lett.* **32**, L14313, (2005).
25. Johnson, L. An earthquake model with interacting asperities. *Geophys. J. Int.* **182**, 1339–1373 (2010).
26. Dreger, D. Nadeau, R. M., & Chung, A. Repeating earthquake finite source models: Strong asperities revealed on the San Andreas Fault. *Geophys. Res. Lett.* **34**, L23302 (2007).
27. Page, M., Dunham, E. & Carlson J. M. Distinguishing barriers and asperities in near-source ground motion, *J. Geophys. Res.* **110**, B11302 (2005).
28. Carpenter, B. M., Marone, C. & Saffer, D. M. Weakness of the San Andreas Fault revealed by samples from the active fault zone. *Nature Geoscience* **4**, 251–254 (2011).
29. Saffer, D. M. & Marone, C. Comparison of smectite- and illite rich gouge frictional properties: Application to the updip limit of the seismogenic zone along subduction megathrusts, *Earth Planet. Sci. Lett.* **215**, 219– 235 (2003).
30. McLaskey, G. C. & Glaser, S. D. Hertzian impact: Experimental study of the force pulse and resulting stress waves. *J. Acoust. Soc. Am.* **128**, 1087–1096 (2010).

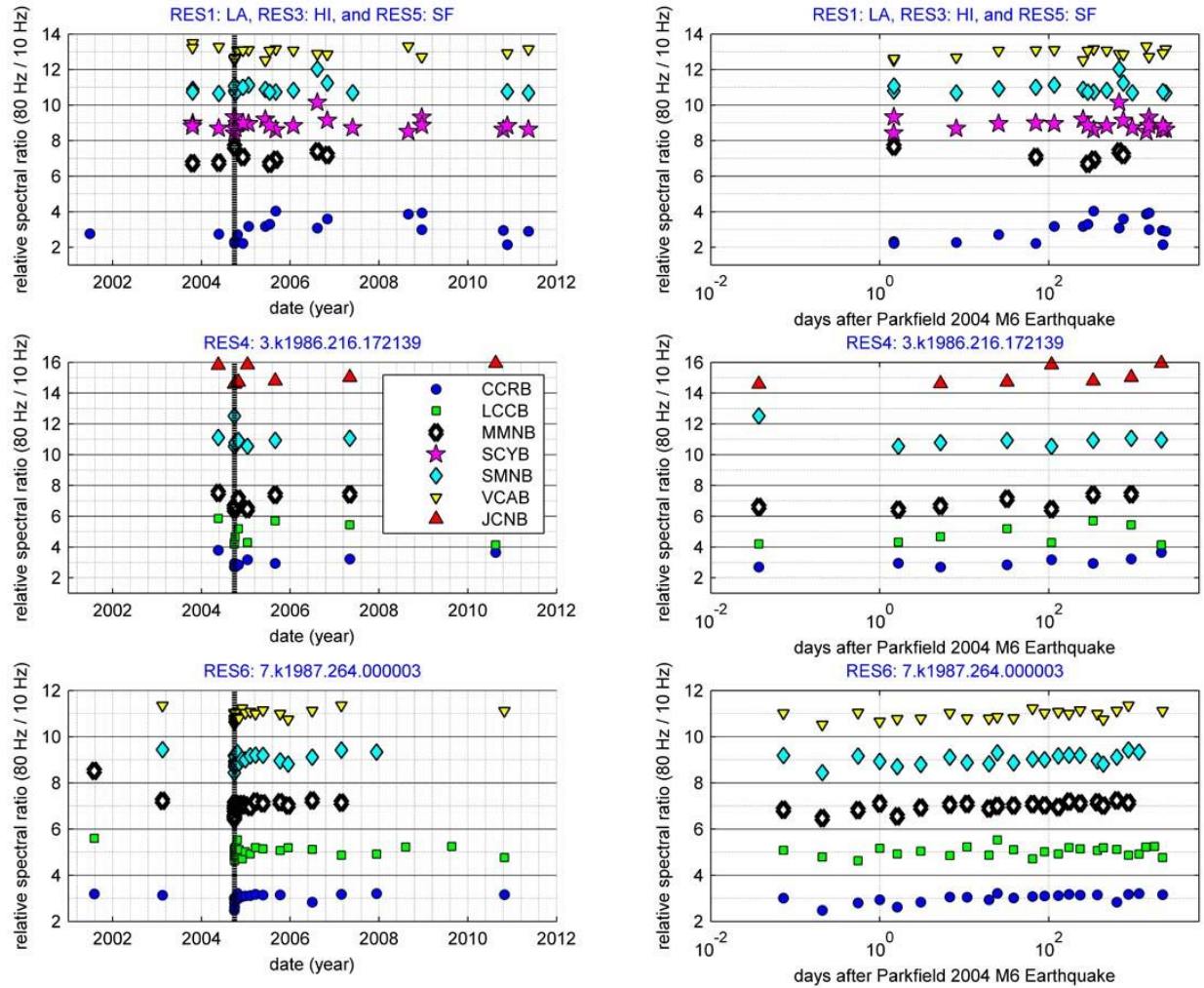
**Acknowledgments** This paper was improved by suggestions from R. Bürgmann and constructive reviews by T. Tullis, C. Marone, W. Ellsworth, and N. Beeler. HRSN data was provided by the Berkeley Seismological Laboratory and NCEDC. Research was supported by the NSF GRF and NSF grants CMMI-1131582, EAR-0738342, and EAR-0910322. This is BSL contribution #11-12.

**Author Contributions** G.C.M. and S.D.G. developed the laboratory experiments. R.M.N. developed and maintained repeating earthquake catalogues. A.M.T. and G.C.M. performed analysis of the RES at Parkfield. G.C.M. performed analysis of LABEQs and wrote the manuscript, with contributions from all authors.

**Author Information:** Reprints and permissions information is available at [www.nature.com/reprints](http://www.nature.com/reprints). The authors declare no competing financial interests. Correspondence and requests for materials should be addressed to G.C.M. (gmclaskey@usgs.gov).

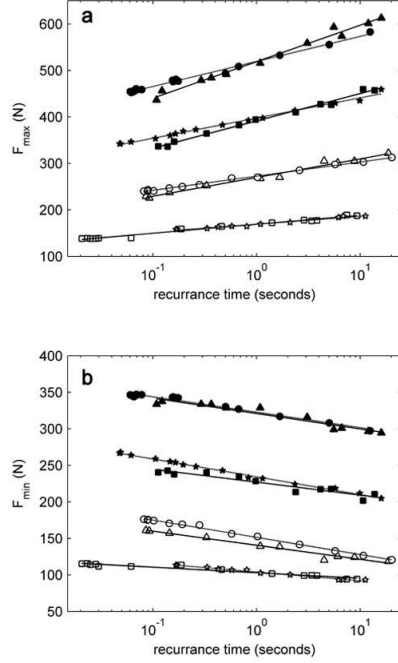


## Supplementary information



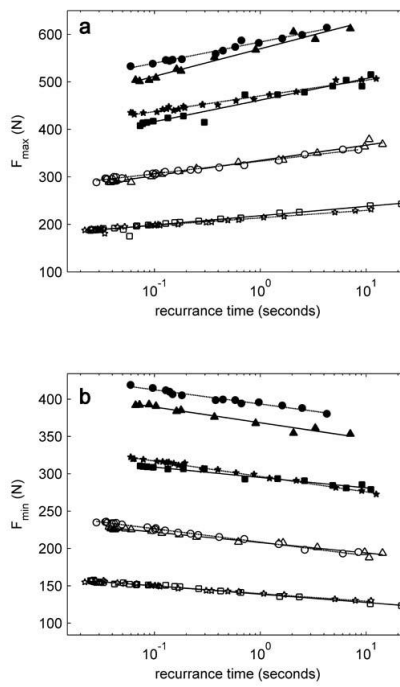
**Supplementary Figure S1.** Comparison of relative spectral levels for the different raypaths. Data points indicate relative spectral ratios (75-85 Hz relative spectral amplitude divided by 5- 15 Hz relative spectral amplitude) from individual station recordings. The scales shown on the y-axes are spectral ratios from between 0 and 2, but each station is offset by an even positive integer (2, 4, 6, etc.). Only ratios obtained from spectra with signal-to-noise ratio greater than 6 dB are shown. The left column shows how relative spectral ratios vary at individual stations as a function of linear time. The time of the Parkfield 2004 M6 earthquake is shown as a vertical dotted line. The right column shows the post-earthquake data on a logarithmic time scale.





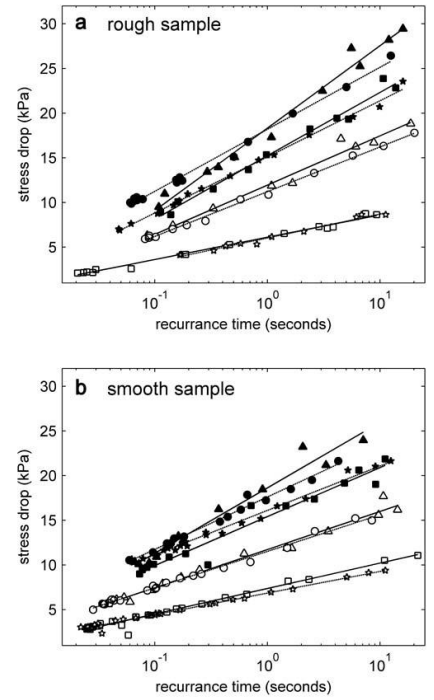
### Supplementary Figure S2.

Experiments on the rough sample at various  $\sigma_n$ . Filled circles and triangles:  $\sigma_n = 130$  kPa; filled stars and squares:  $\sigma_n = 96$  kPa; open circles and triangles:  $\sigma_n = 61$  kPa; open stars and squares:  $\sigma_n = 36$  kPa. Triangles and squares indicate events from runs with decreasing load point velocity while circles and stars are from runs with increasing load point velocity. In all cases, parameters are observed to vary linearly with  $\log_{10}(t_r)$ . Best-fit lines for each run are also plotted. Slope,  $\beta$ , and intercept,  $\alpha$ , of these lines are listed in Table S1.



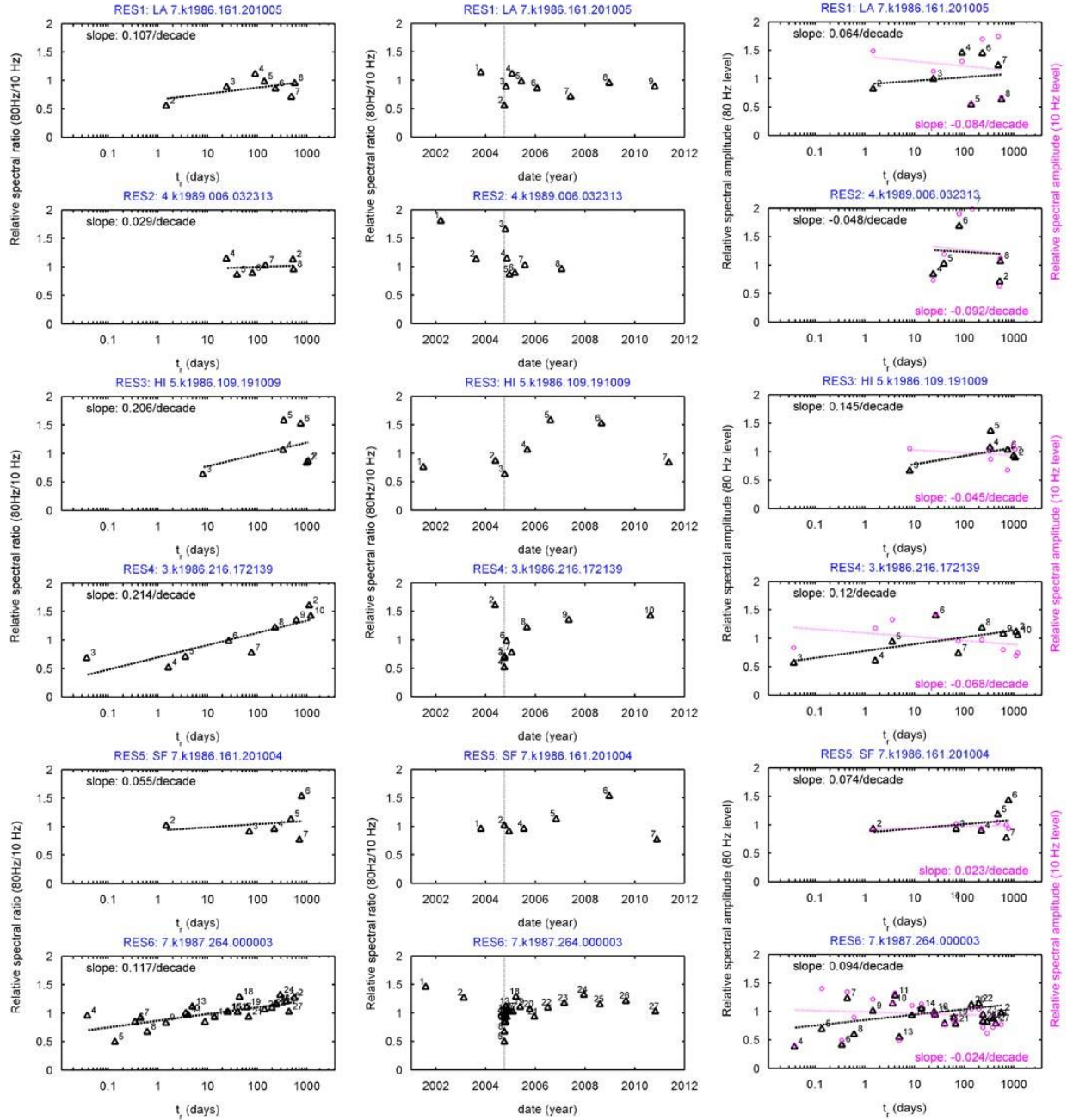
### Supplementary Figure S3.

Experiments on the smooth sample at various  $\sigma_n$ . Filled circles and triangles:  $\sigma_n = 130$  kPa; filled stars and squares:  $\sigma_n = 96$  kPa; open circles and triangles:  $\sigma_n = 61$  kPa; open stars and squares:  $\sigma_n = 36$  kPa. Triangles and squares indicate events from runs with decreasing load point velocity while circles and stars are from runs with increasing load point velocity. In all cases, parameters are observed to vary linearly with  $\log_{10}(t_r)$ . Best-fit lines for each run are also plotted. Slope,  $\beta$ , and intercept,  $\alpha$ , of these lines are listed in Table S1.

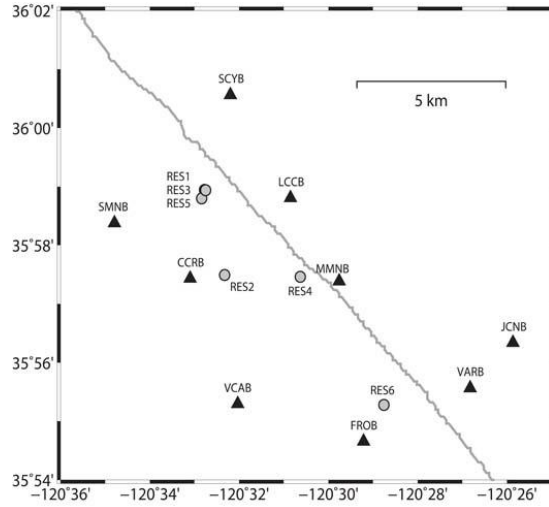


### Supplementary Figure S4.

Measured  $\Delta\tau$  for all experimental runs. Filled circles and triangles:  $\sigma_n = 130$  kPa; filled stars and squares:  $\sigma_n = 96$  kPa; open circles and triangles:  $\sigma_n = 61$  kPa; open stars and squares:  $\sigma_n = 36$  kPa. Triangles and squares indicate events from runs with decreasing load point velocity while circles and stars are from runs with increasing load point velocity.



**Supplementary Figure S5.** Relative spectral levels and ratios for the six RES analyzed in this study. Data points denote the average of relative spectral ratios (left and center columns) or relative spectral amplitudes at 75–85 Hz and 5–15 Hz (right column) obtained from ground motions recorded from at least three stations for each event in each RES. Only spectra with signal-to-noise ratio greater than 6 dB are used. Left: ratio of 75–85 Hz relative spectral amplitudes to 5–15 Hz spectral amplitudes (same as shown in Figure 4). Numbers next to each symbol indicate the order of events in each RES. Center: relative spectral ratios as a function of linear time. The time of the Parkfield 2004 M6 earthquake is shown as a vertical dotted line. Right: The relative spectral amplitudes at 5–15 Hz (magenta circles) can be used as a proxy for relative seismic moment. Black triangles show relative spectral amplitudes at 75–85 Hz.



**Supplementary Figure S6.** RES and HRSN station locations. RES and HRSN stations used in this study are shown as gray circles and black triangles respectively. The San Andreas fault trace is shown in gray.

**Supplementary Table S1.** Static strength and healing parameters. Parameters are the results of 16 experimental runs on smooth (S) and rough (R) sample blocks and four different levels of  $\sigma_n$ . Variation in strength with recurrence time were studied by systematically increasing (Inc) or decreasing (Dec) the load point velocity during an experimental run.  $\beta$  is the slope and  $\alpha$  is the intercept (at  $t_r = 1$  s) of best fit lines of the various parameters plotted against  $\log_{10}(t_r)$ . The apparatus/specimen stiffness is calculated from a plot of  $(F_{\max} - F_{\min})$  versus  $\delta_T$  and is the slope of the best-fit line through the origin and each individual event in an experimental run.

Run Name	$\sigma_n$	$\alpha_{F_{\max}}$	$\beta_{F_{\max}}$	$\alpha_{F_{\min}}$	$\beta_{F_{\min}}$	$\alpha_s = \alpha_{F_{\max}} / F_n$	$\beta_s = \beta_{F_{\max}} / F_n$	$\alpha_{\Delta\tau} / \sigma_n$	$\beta_{\Delta\tau} / \sigma_n$	stiffness
	(kPa)	(N)	(N/decade)	(N)	(N/decade)	(dimensionless)	(decade <sup>-1</sup> )	(dimensionless)	(decade <sup>-1</sup> )	(N/ $\mu$ m)
Run 30 S Dec	36.4	218.4	19.6	138.8	-11.1	0.55	0.049	0.2	0.078	1.4
Run 31 S Inc	36.4	213.9	15.9	139.8	-10.3	0.54	0.040	0.19	0.067	1.4
Run 28 S Dec	61.1	334.6	32.1	207.9	-13.9	0.50	0.048	0.19	0.07	1.6
Run 29 S Inc	61.1	333.1	26.2	208.5	-17.9	0.50	0.039	0.19	0.067	1.6
Run 24 S Dec	95.8	461.6	45.3	295	-13.9	0.44	0.043	0.16	0.057	2.0
Run 25 S Inc	95.8	470.6	33	296.5	-20.6	0.45	0.032	0.17	0.052	1.9
Run 18 S Dec	130.5	569.6	58	368.3	-21	0.40	0.041	0.14	0.056	2.4
Run 19 S Inc	130.5	583.9	44.4	393.5	-19	0.41	0.031	0.14	0.045	2.5
Run 35 R Dec	36.4	169.0	19.3	103	-7.6	0.43	0.049	0.17	0.068	1.4
Run 36 R Inc	36.4	169.3	16.9	104.1	-12	0.43	0.043	0.17	0.074	1.5
Run 38 R Dec	61.1	269.7	40.2	140.6	-19.3	0.40	0.060	0.2	0.09	1.1
Run 39 R Inc	61.1	272.7	30.5	151.5	-23.6	0.41	0.046	0.18	0.082	1.2
Run 43 R Dec	95.8	391.5	58.8	226.9	-17.7	0.37	0.056	0.16	0.074	1.2
Run 44 R Inc	95.8	397.6	43.4	234.4	-24.4	0.38	0.042	0.16	0.066	1.3
Run 45 R Dec	130.5	518.9	78.5	320.9	-21.1	0.36	0.055	0.14	0.071	1.5
Run 46 R Inc	130.5	519.5	53.9	322.9	-21.1	0.37	0.038	0.14	0.053	1.6

Supplementary Table S2. RES information.				
RES Name	Longitude	Latitude	Depth (km)	Mean Magnitude
RES 1: LA	-120.546191	35.98243	2.31	1.861
RES 2	-120.538737	35.958297	10.83	1.45
RES 3: HI	-120.547249	35.98007	2.159	1.859
RES 4	-120.51046	35.95775	8.87	2.06
RES 5: SF	-120.545833	35.982365	2.09	2.096
RES 6	-120.479224	35.921346	3.899	1.222

Supplementary Table S3. RES event information.					
RES	Event #	Year	Day	HHMMSS.SS	Magnitude
RES1: LA	1	2003	294	90012.64	1.87
RES1: LA	2	2004	274	43449.98	1.9
RES1: LA	3	2004	298	85256.35	1.821
RES1: LA	4	2005	23	75352.24	1.861
RES1: LA	5	2005	161	114537.07	1.639
RES1: LA	6	2006	28	1751.64	1.96
RES1: LA	7	2007	150	104921.25	1.973
RES1: LA	8	2008	354	103217.83	1.696
RES1: LA	9	2010	294	3908.87	1.5
RES2	1	2002	70	171506.63	1.112
RES2	2	2003	224	152505.82	1.131
RES2	3	2004	288	22301.22	0.854
RES2	4	2004	312	20226.9	1.175
RES2	5	2004	351	140023.8	1.308
RES2	6	2005	65	43701.4	1.449
RES2	7	2005	211	113210.76	1.45
RES2	8	2007	19	161355.89	1.292
RES3:HI	1	2001	178	53408.55	1.753
RES3:HI	2	2004	145	5408	1.859
RES3:HI	3	2004	280	190312.36	1.848
RES3:HI	4	2005	247	61005.09	1.859
RES3:HI	5	2006	223	92737.75	1.808
RES3:HI	6	2008	242	102128.83	1.831
RES3:HI	7	2011	135	163451.55	1.856
RES4	1	2001	125	344.04	2.03
RES4	2	2004	139	65232.36	1.94
RES4	3	2004	272	180901.66	2.13
RES4	4	2004	274	91103.86	2.24
RES4	5	2004	277	232641.71	2.27
RES4	6	2004	304	212154.16	2.28
RES4	7	2005	15	33158.65	2.14
RES4	8	2005	242	34242.78	2.15
RES4	9	2007	125	203400.82	2.09

RES4	10	2010	231	10923.9	2
RES5: SF	1	2003	293	112543.01	2.136
RES5: SF	2	2004	274	43641.97	2.08
RES5: SF	3	2004	343	71645.9	2.114
RES5: SF	4	2005	197	33309.45	2.096
RES5: SF	5	2006	306	14022.95	2.128
RES5: SF	6	2008	355	62215.57	2.161
RES5: SF	7	2010	327	2055.89	2.079
RES6	1	2001	214	152321.07	0.935
RES6	2	2003	46	92404.31	1.106
RES6	3	2004	272	180445.81	1.295
RES6	4	2004	272	185944.88	0.943
RES6	5	2004	272	221646.33	1.297
RES6	6	2004	273	63618.49	1.005
RES6	7	2004	273	171954.58	1.286
RES6	8	2004	274	75805.5	1.174
RES6	9	2004	275	185523.37	1.258
RES6	10	2004	279	110549.58	1.24
RES6	11	2004	283	125702.53	1.28
RES6	12	2004	292	100723.71	1.233
RES6	13	2004	297	92041.2	1.013
RES6	14	2004	311	61714.47	1.243
RES6	15	2004	337	72253.42	1.19
RES6	16	2004	362	65932.61	1.2
RES6	17	2005	36	145155.8	1.138
RES6	18	2005	80	124615.18	1.217
RES6	19	2005	142	54207.68	1.147
RES6	20	2005	282	114513.41	1.222
RES6	21	2005	349	62649.91	1.158
RES6	22	2006	182	55534.88	1.226
RES6	23	2007	57	80856.04	1.147
RES6	24	2007	346	130500.28	1.127
RES6	25	2008	220	131147.35	1.143
RES6	26	2009	234	114951.8	1.156
RES6	27	2010	302	225226.67	1.128